Theoretical and Applied Mechanics Letters 15 (2025) 100608

Contents lists available at ScienceDirect

Theoretical and Applied Mechanics Letters

journal homepage: www.elsevier.com/locate/taml

Computational study on the fluid-structure interaction between explosion-induced bubbles and submarine pipes

Lei Gao[a], Junjie Zhao[b,*], Maoyu Qi[b], Wentao Ma[c], Shunxiang Cao[b]

[a] Offshore Engineering Solution Co., Ltd., China National Offshore Oil Corporation, Shenzhen 518052, China
[b] Institute for Ocean Engineering, Shenzhen International Graduate School, Tsinghua University, Shenzhen 518055, China
[c] Department of Bioengineering, School of Medicine, Duke University, Durham 27708, USA

ARTICLE INFO

Keywords:
Fluid–structure interaction
Underwater explosion
Submarine pipeline
Bubble dynamics

ABSTRACT

Submarine pipelines are critical infrastructures for offshore energy transport and communications. Understanding their structural response to near-field explosions is crucial for enhancing their blast resistance and operational safety. This study presents a computational study on the interaction between explosion-induced bubbles and a seabed-mounted pipeline. A recently developed computational framework is employed, which couples a compressible fluid solver with a finite element structural solver via a partitioned procedure. An embedded boundary method and a level-set method are employed to handle the fluid-structure and gas-liquid interfaces. Using this framework, we analyze the flow field evolution, bubble dynamics, and transient pipe deformation. Two distinct response modes are identified: periodic oscillation under low-pressure loading and downward collapse triggered by high-pressure loading and bubble jet impact. Specifically, under high-pressure conditions, the pipe initially deforms inward, generating a localized high-pressure zone within the concave region. During structural rebound, the trapped fluid is expelled upward, giving rise to a bubble jet. Further parametric studies on the pipe's internal pressure, wall thickness, and support angle reveal several key insights. A higher internal pressure delays structural collapse, and a greater pipe thickness results in more uniform implosion morphologies. The support angle strongly influences the collapse dynamics, with the shortest collapse time occurring at 60°. These findings offer new insights for the protective design of submarine pipelines.

1. Introduction

Submarine pipelines are critical components of ocean engineering, and serves as essential infrastructures for energy transportation [1,2], deep-sea resource development [3,4], and transoceanic communication [5]. These pipelines operate in complex marine environments, where they must endure long-term exposure to ocean currents and corrosion, as well as sudden extreme events such as underwater explosions. A prominent example is the Nord Stream pipeline incident in 2022, where a suspected underwater explosion led to catastrophic pipeline rupture, leading to major environmental and geopolitical consequences. Understanding the dynamic response of submarine pipelines to underwater explosions is essential for improving blast-resistant designs and ensuring the reliability of key national infrastructures [6].

Underwater explosions are typically categorized into far-field [7] or near-field [8] scenarios on the basis of the distance between the explosion source and the submarine structure [9]. In far-field explosions [7], the explosion-induced shock wave gradually attenuates into linear acoustic waves during propagation. This phenomenon primarily induces global structural responses through hydrodynamic impact loading. To assess potential damage, researchers often simplify these shock waves via one-dimensional hydrodynamic models [8,10]. In contrast, near-field explosions are far more complex and involve three primary loading mechanisms: the initial shock wave, pressure pulsations from bubble oscillation, and high-speed jets formed during nonspherical bubble collapse [11,12]. Moreover, the shockwave-bubble-structure interaction further generates rarefaction waves [13], creating an intermediate cavitation zone with subatmospheric pressures [14]. The subsequent collapse of cavitation bubbles within this region produces secondary impacts that impose cyclic loads on nearby structures. Experimental investigations by Brett et al. [15,16] have quantitatively demonstrated the critical role of cavitation-induced loads in governing the deformation patterns of submerged cylindrical structures.

In near-field scenarios, jet pressures generated by bubble collapse [17] can exceed the initial shock wave magnitude. Such extreme loading often leads to severe deformation in submarine pipelines accompanied by nonlinear material phenomena, including yielding and fracturing [18–22]. Although the collapse mechanisms of cylindrical shells

* Corresponding author.
E-mail address: zjj23@mails.tsinghua.edu.cn (J. Zhao).

https://doi.org/10.1016/j.taml.2025.100608
Received 4 May 2025; Received in revised form 4 July 2025; Accepted 4 July 2025
Available online 8 July 2025

under hydrostatic compression have been extensively investigated [23–26], their dynamic response to near-field blast loading remains less explored. Gupta et al. [18] performed experiments on the collapse of 6061-T6 aluminum pipes in a confined environment, where the samples were subjected to combined loading from preapplied hydrostatic pressure and longitudinal explosion. Their results revealed that the pressure pulse induced by the initial collapse of the explosion bubble exerted a non-negligible influence on the structure. Later, Sun et al. [27] conducted numerical simulations and theoretical modeling to reveal how the initial hydrostatic pressure and fluid-structure interaction influence the stability of cylindrical metal shells. Their findings demonstrated that pre-existing hydrostatic pressures degrade structural stiffness, triggering a progression from axisymmetric vibration to secondary vibration modes. A critical pressure threshold was identified, beyond which shell implosion occurred abruptly. More recent experimental work by Mao et al. [28] further investigated the role of internal pressures and wall thicknesses on thickness in the deformation and damage of pressurized cylindrical shell pipes. They revealed that higher initial internal pressures enhanced the structural resistance, whereas increased wall thickness unexpectedly reduced it. Research [29] revealed a two-stage deformation pattern of the pipe: minor initial distortion during the shock wave stage, followed by significantly amplified deformation during the bubble pulsation stage. Recently, Ma et al. [9] conducted numerical studies on the dynamic coupling mechanisms between underwater explosion bubbles and unrestrained pipes, analyzing the bidirectional interaction between bubbles and structural dynamics. They reported that at relatively low amplitudes, cylindrical shells collapsed in a counterintuitive manner and noted that the collapse time did not monotonically decrease with increasing explosion amplitude.

While significant progress has been made in understanding pipeline dynamics. Most existing studies—primarily aimed at enhancing structural blast resistance via modifications in structural configurations and material properties [30,31]—have relied on idealized models and have not fully accounted for three critical factors relevant to practical applications: seabed constraints, the two-way interaction between bubble dynamics and the pipe response, and structural support configurations. These factors introduce substantial complexity into the fluid-structure interaction behavior of the pipe. To fill this knowledge gap, this study investigates the dynamic response of a seabed-mounted pipe subjected to near-field explosions. We employed a recently developed multiphase fluid-structure interaction solver to capture the two-way interaction between bubble dynamics and the structural response. For a given explosion pressure, we systematically analyze the effects of the internal pipe pressure, pipe wall thickness, and support angle on the implosion resistance of seabed pipes. These findings provide a theoretical foundation for optimizing pipeline design and enhancing structural resilience under explosive loading. The paper is organized as follows: Section 2 introduces the physical model and numerical methods, including a mesh convergence analysis for verification. In Section 3, we analyze the dynamic response of pipes under different underwater explosion bubble pressures. Section 4 explores the implosion resistance of seabed pipes with varying internal pressures, wall thicknesses, and support angles under near-field underwater explosions. Finally, concluding remarks are presented in Section 5.

2. Mathematical model and numerical methods

2.1. Problem description

Figure 1 shows the physical model of an underwater explosion in proximity to the pipeline considered in this study. A thin-walled cylindrical pipe filled with air is submerged in high-pressure water and supported by a rigid seabed through a symmetric support structure. Near-field explosion occurs above the pipe and is modeled as a high-pressure gas bubble. As shown in Table 1, δ denotes the thickness of the pipe wall, d_b is the vertical distance between the centers of the bubble and the pipe, and d_w is the distance from the pipe center and the seabed. The angle between two supports is denoted by α, while R_s and R_b denote the inner radius of the pipe and the initial radius of the bubble, respectively. The geometric properties of the pipe follow those used in Zhao and Lam et al. [32,33], and serve as the baseline parameters, as summarized in Table 1. In subsequent parametric studies, individual parameters are systematically varied from these reference values to evaluate their influence on the bubble-pipe interaction.

Table 1
Geometric properties of the proposed model.

Symbol	Properties	Value
δ	Pipe's thickness (mm)	20
d_w	Pipe-seabed distance (mm)	600
R_s	Pipe's inner radius (mm)	500
d_b	Bubble-pipe distance (mm)	750
α	Supports' angle (°)	60
R_b	Bubble's initial radius (mm)	50

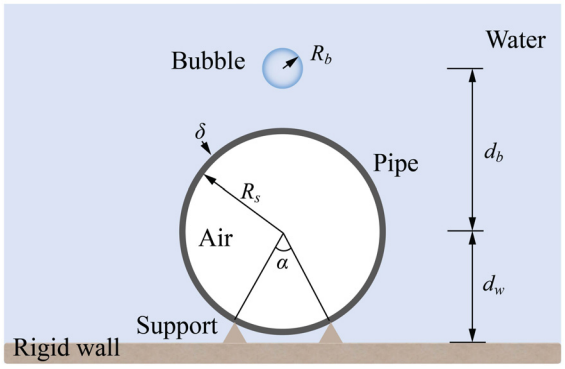

Fig. 1. Schematic of bubble explosion dynamics analysis with a pipe.

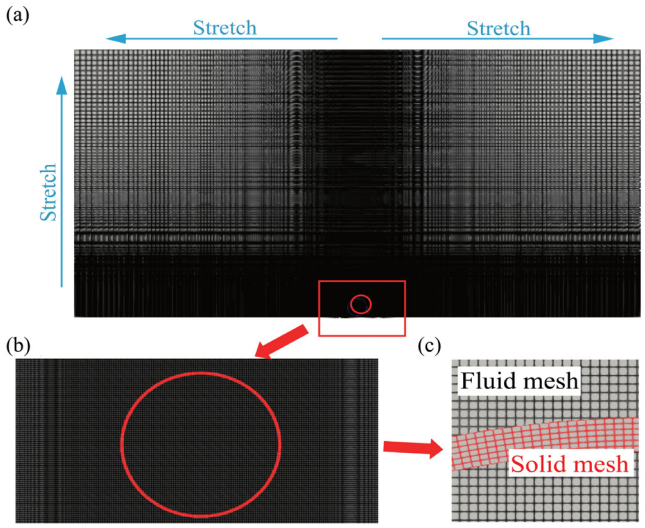

Fig. 2. Diagrams of grid division: (a) overall mesh, (b) grid near the pipe, and (c) interface of the fluid and solid mesh.

The entire computational domain is shown in Fig. 2, with a length of 60 times the pipe radius and a width of 30 times the pipe radius. Farfield boundary conditions are applied to the left, right, and upper boundaries of the fluid domain, whereas the lower boundary is treated as a rigid seabed and modeled as a wall boundary condition. A dense mesh is used near the pipe and the bubble within the fluid computational domain, which is stretched toward the boundaries to improve computational efficiency. The solid computational mesh, shown as the red grid

in Fig. 2(c), adopts a structured and uniformly divided grid for the pipe. The inner and outer contact surfaces are set as embedded boundaries for fluid-structure coupling.

2.2. Governing equations and discretization

2.2.1. Governing equations

In this study, both the gas inside the bubble and the pipe, as well as the surrounding water, are modeled as compressible inviscid fluids. The omission of viscosity can be explained by the dominance of high-pressure shock waves generated during underwater explosions. Hence, the governing equations for the liquid and gas are the following Euler equations:

$$\frac{\partial \boldsymbol{W}(\boldsymbol{x},t)}{\partial t} + \nabla \cdot \boldsymbol{\mathcal{F}}(\boldsymbol{W}) = \boldsymbol{0}, \quad \forall\, \boldsymbol{x} \in \Omega_{L(t)} \cup \Omega_{G(t)},\ t > 0 \tag{1}$$

with

$$\boldsymbol{W} = \begin{bmatrix} \rho \\ \rho \boldsymbol{V} \\ \rho e_t \end{bmatrix}, \quad \mathcal{F} = \begin{bmatrix} \rho \boldsymbol{V}^{\mathrm{T}} \\ \rho \boldsymbol{V} \otimes \boldsymbol{V} + p\boldsymbol{I} \\ (\rho e_t + p)\boldsymbol{V}^{\mathrm{T}} \end{bmatrix}, \tag{2}$$

where ρ, e_t, and p represent the mass density, total energy per unit mass, and pressure, respectively. The velocity vector is denoted as $\boldsymbol{V} = (u, v, w)^{\mathrm{T}}$. The total energy per unit mass, e_t, can be expressed as follows:

$$e_t = e + \frac{1}{2}|\boldsymbol{V}|^2, \tag{3}$$

where e represents the internal energy per unit mass. We utilize the equations of state for different fluid materials to close the Euler equations. Specifically, the Tait equation of state is employed for the liquid water

$$p = p_c + \alpha \left[\left(\frac{\rho}{\rho_c} \right)^{\beta} - 1 \right], \tag{4}$$

where the parameters are set as $\alpha = 3.5291 \times 10^8$ and $\beta = 6.4762$ [34]. Here, the reference state density and pressure are set to $\rho_c = 1.0 \times 10^3\,\mathrm{kg{\cdot}m^{-3}}$ and $p_c = 1.0 \times 10^5\,\mathrm{Pa}$, respectively. The ideal gas equation of state is employed for the air inside the bubble and the pipe:

$$p = (\gamma - 1)\rho e, \tag{5}$$

where the specific heat ratio γ is set to 1.4 in this study.

In this work, the initial densities inside the explosion bubble and the pipe are set to $50\,\mathrm{kg{\cdot}m^{-3}}$ and $1.225\,\mathrm{kg{\cdot}m^{-3}}$, respectively. The initial bubble pressure P_b and the initial pressure inside the pipe P_i are treated as variable parameters to investigate their effects on the structural response. For the baseline case, $P_i = 10^5$ Pa.

For the structural model, we follow our previous work by Cao et al. [35], in which we adopt a Lagrangian approach to model the dynamic equilibrium of the cylindrical pipe within the solid domain:

$$\rho_s \ddot{\boldsymbol{u}}(\boldsymbol{X},t) - \nabla \cdot \left(\boldsymbol{J}^{-1}\boldsymbol{G} \cdot \boldsymbol{S} \cdot \boldsymbol{G}^{\mathrm{T}} \right) = \boldsymbol{b}, \tag{6}$$

where ρ_s represents the density of the solid material, $\boldsymbol{u}$ denotes the displacement vector, $\boldsymbol{X}$ represents the material coordinate, $\boldsymbol{S}$ represents the second Piola-Kirchhoff stress tensor, $\boldsymbol{G}$ represents the deformation gradient, and $\boldsymbol{J} = \det \boldsymbol{G}$. The body force $\boldsymbol{b}$ is assumed to be zero in this study. We consider a pipe built with elastoplastic aluminum alloy [36], which is capable of yielding and undergoing plastic deformation. The J_2 isotropic hardening flow theory is used, and the yield criterion is defined as follows:

$$\sqrt{2J_2(\mathbf{s})} = \left(\frac{3}{2}\mathbf{s} \cdot \mathbf{s} \right)^{1/2} = \sigma_e, \tag{7}$$

where $\mathbf{s}$ represents the deviatoric part of the second Piola-Kirchhoff stress tensor, and σ_e is the von Mises effective stress. Specifically, the material properties of the pipe are consistent with those of previous studies [9,36]. The aluminum alloy has the Young's modulus of 69.6 GPa, density of $2779\,\mathrm{kg{\cdot}m^{-3}}$, Poisson's ratio of 0.33, tangent modulus of 674 MPa, and yield stress of 292 MPa.

On the fluid-structure interface Ω_{FS}, the normal velocity and surface traction are continuous, leading to the following interface conditions:

$$\begin{aligned} &(\boldsymbol{V} - \dot{\boldsymbol{u}}) \cdot \boldsymbol{n} = 0, \\ &-p\boldsymbol{n} = \boldsymbol{\sigma} \cdot \boldsymbol{n}, \end{aligned} \tag{8}$$

where $\boldsymbol{n}$ denotes the unit normal vector to the interface, and $\boldsymbol{\sigma}$ represents the Cauchy stress tensor. The relationship between the Cauchy stress tensor and the second Piola-Kirchhoff stress tensor is given by: $\boldsymbol{\sigma} = \boldsymbol{J}^{-1}\boldsymbol{G} \cdot \boldsymbol{S} \cdot \boldsymbol{G}^{\mathrm{T}}$

The bubble surface Ω_{LB} is assumed to be immiscible. Moreover, compared with the dynamic pressure of the fluid, the surface tension of the bubble can be neglected. Hence, it can be assumed that the normal velocity and pressure are continuous across Ω_{LB}. We track the evolution of the gas-liquid interface by solving the level-set equation:

$$\frac{\partial \phi(\boldsymbol{x},t)}{\partial t} + \boldsymbol{V} \cdot \nabla \phi = 0, \tag{9}$$

where $\phi(\boldsymbol{x},t)$ represents the level-set function, which is initialized as the shortest distance from point $\boldsymbol{x}$ to the interface. This approach naturally accommodates complex deformations and topological changes in the bubble surface, such as splitting or merging, do not require special treatment.

2.2.2. Numerical discretization

In this study, a recently developed fluid-structure interaction computational framework is utilized to solve the above model equations. Figure 3 and Algorithm 1 illustrate the spatial and temporal discretization methods employed in this framework. For each grid node (node i),

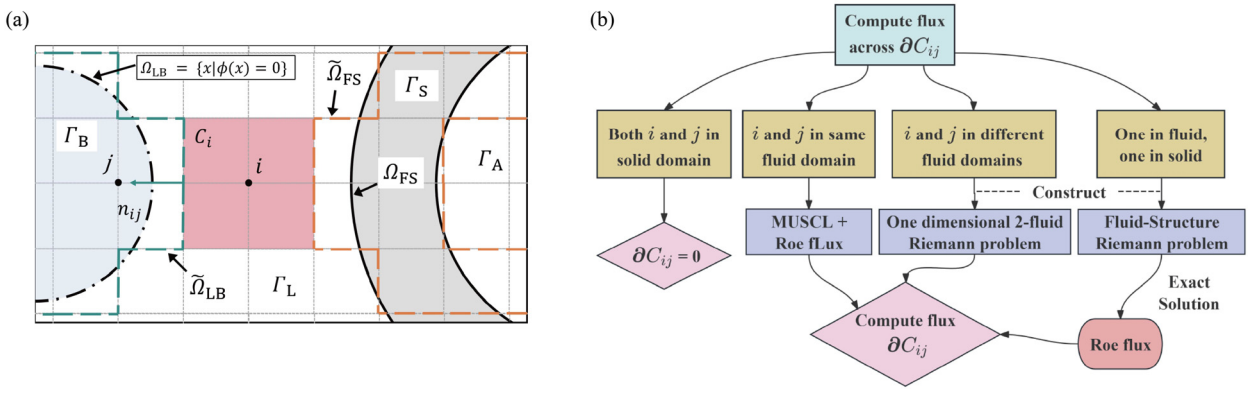

Fig. 3. Illustration of the (a) space discretization and (b) surface flux integral methods applied in the computational framework.

Algorithm 1 Partitioned Procedure for Fluid-Structure Coupling

Input: Initial states $W^{h,n}$, $\boldsymbol{u}^{h,n+1/2}$
Initialization:
for $n = 0$ to $n_{\text{steps}} - 1$ **do**
  Step 1: Multiphase Fluid Dynamics Solver
  Compute $W^{h,n+1}$:

$$W^{h,n+1} \leftarrow \text{Fluid Solver}(W^{h,n}, \boldsymbol{u}^{h,n+1/2}, \dot{\boldsymbol{u}}^{h,n+1/2})$$

  Step 2: Solid Dynamics Solver (First Half)
  Compute updated velocity $\boldsymbol{u}^{h,n+3/2}$:

$$\boldsymbol{u}^{h,n+3/2} \leftarrow \text{Solid Solver}(\boldsymbol{u}^{h,n+1/2}, f^{\text{ext},n+1}, W^{h,n+1})$$

  Step 3: Multiphase Fluid Dynamics Solver (Next Step)
  Compute $W^{h,n+2}$:

$$W^{h,n+2} \leftarrow \text{Fluid Solver}(W^{h,n+1}, \boldsymbol{u}^{h,n+3/2}, \dot{\boldsymbol{u}}^{h,n+3/2})$$

end for

a control volume C_i is constructed. By integrating Eq. (1) over C_i, the following form is obtained:

$$\frac{\partial W_i}{\partial t} + \frac{1}{\|C_i\|} \sum_{j \in Nei(i)} \int_{\partial C_{ij}} \boldsymbol{\mathcal{F}}(\boldsymbol{W}) \cdot \boldsymbol{n}_{ij} \mathrm{d}S = 0, \tag{10}$$

where W_i represents the average value of each component of $\boldsymbol{W}$ at C_i, $||C_i||$ denotes the volume of C_i, $Nei(i)$ refers to the set of neighboring nodes connected to node i by an edge, and $\partial C_{ij} = \partial C_i \cap \partial C_j$. The vector $\boldsymbol{n}_{ij}$ is the unit normal vector perpendicular to ∂C_i. Depending on the relative positions of nodes i and j, four different scenarios may arise when calculating the surface integral on ∂C_i. (a) If both nodes i and j lie within the solid domain, then ∂C_{ij} is set to zero. (b) When nodes i and j belong to the same fluid domain (Γ_{L}, Γ_{A}, Γ_{B}), the flux passing through ∂C_{ij} is computed via the monotonic upstream-centered scheme for conservation laws (MUSCL) [37] and the Roe flux function [38]. (c) If nodes i and j belong to different fluid domains (e.g., one in Γ_{L} and the other in Γ_{B}), a one-dimensional two-fluid Riemann problem is constructed along the i-j edge. (d) When one node belongs to the fluid domain and the other belongs to the solid domain, a one-dimensional fluid-structure Riemann problem with a moving wall boundary is constructed. The exact solution of this problem is then provided to the Roe flux function to compute the flux passing through ∂C_{ij}.

For structural discretization, the weak form of Eq. (6) is semidiscretized via the Galerkin finite element method, yielding:

$$\boldsymbol{M} \frac{\partial^2 \boldsymbol{u}^h}{\partial t^2} + \boldsymbol{f}^{\text{int}}\left(\boldsymbol{u}^h, \frac{\partial \boldsymbol{u}^h}{\partial t}\right) = \boldsymbol{f}^{\text{ext}}, \tag{11}$$

where $\boldsymbol{M}$ represents the mass matrix; $\boldsymbol{u}^h$ denotes the discrete displacement vector; and $\boldsymbol{f}^{\text{int}}$ and $\boldsymbol{f}^{\text{ext}}$ represent the discrete internal force vector and external force vector, respectively. In this study, we employ the staggered fluid-structure time integration algorithm proposed by Farhat et al. [39] to solve the coupled fluid dynamics and structural mechanics equations. The fluid equations are time-integrated via an explicit fourth-order Runge-Kutta method, whereas the structural equations are integrated using a second-order central difference scheme. As shown in Algorithm 1, the time steps for the fluid and solid are staggered by half a step. This design ensures second-order accuracy in time integration while maintaining numerical stability.

2.3. Verification and validation of the computational framework

The computational framework employed in this study was thoroughly validated in our previous work across a wide range of relevant physical processes, including fluid-structure interactions [36,40–44], bubble dynamics [45], and multiphase gas-liquid coupling [46,47]. This method has demonstrated excellent agreement with experimental results in terms of deformation morphology, pressure evolution, and interface tracking [9,34,48,49]. In the absence of experimental data, exactly matches our simulation setup, we validate our numerical model by comparing it against both the numerical and experimental results reported by Ma et al. [9], using identical parameter settings. As shown in Fig. 4, our simulation results (Fig. 4(a)) strongly agree with both prior numerical results (Fig. 4(b)) and experimental observations (Fig. 4(c)) in terms of bubble dynamics and structural deformation. Our model accurately reproduces the upward counterjet and the "counterintuitive" deformation pattern observed in the reference study. The bubble interface in our simulations appears smoother than that in previous studies, which we attribute to the locally initialized level-set method employed in our framework. This technique enhances the interface resolution and solution efficiency. These findings confirm the validity of our numerical approach in capturing key features of fluid-structure interactions.

A mesh convergence analysis is then conducted for the configuration shown in Fig. 2. Four levels of grid density are tested in the refined region of the fluid domain: 117,375 (fluid mesh 1), 209,000 (fluid mesh 2), 468,874 (fluid mesh 3), and 1,881,000 (fluid mesh 4). The mesh outside the refined zone is scaled proportionally. For each fluid mesh, three solid mesh densities are evaluated: 2,560 (solid mesh 1), 3,840 (solid mesh 2), and 5120 (solid mesh 3).

Figure 5 compares the resulting collapse times of the pipe for all the tested meshes. As the fluid mesh is refined, clear convergence can be observed. For a fixed fluid mesh, variations in the solid mesh lead to only minor fluctuations in the collapse time, with convergence also achieved across solid mesh levels. When fluid mesh 3 and solid mesh 2 are used, the influence of further grid refinement on the collapse time becomes negligible. Therefore, fluid mesh 3 and solid mesh 2 are selected for the subsequent simulations, balancing accuracy and computational efficiency.

3. Pipe response under different explosion pressures

In an underwater explosion, the explosive charge determines the initial internal pressure of the bubble, which in turn affects the bubble's expansion dynamics, including volume evolution, maximum radius, and oscillation period. The resulting pressure waves and fluid motions then govern the impact force and collapse behaviors of nearby pipes. Hence,

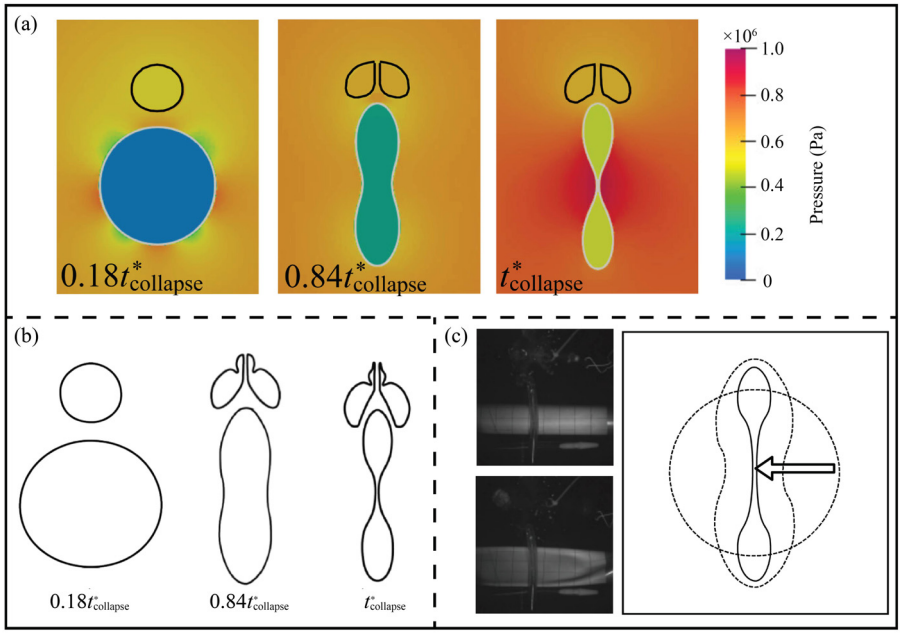

Fig. 4. Comparison of bubble–pipe interactions: (a) present simulation results; (b) reference simulation results [9]; (c) experimental observations [50].

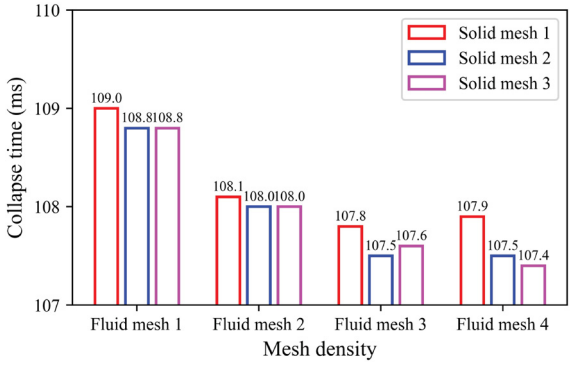

Fig. 5. Results of the grid independence test under 4 fluid mesh densities and 3 solid mesh densities.

a systematic analysis is carried out to investigate how varying the initial pressure of a bubble affects the structural response of the pipe. Seven different pressures are examined: P_b = 10, 25, 30, 35, 50, 75, 100, 150, and 200 MPa. This study focuses on the fluid-structure interaction following bubble formation without explicitly modeling the detonation process. To represent varying explosion intensities in a parametric manner, swe use the Jones–Wilkins–Lee (JWL) equation [51] to map bubble internal pressures to equivalent TNT charges:

$$P = A_1\left(1-\frac{\omega}{R_1V}\right)e^{-R_1V} + B_1\left(1-\frac{\omega}{R_2V}\right)e^{-R_2V} + \frac{\omega E}{V}, \tag{12}$$

where A_1, R_1, B_1, R_2, and ω are material-specific constants; and V and E are the dimensionless specific volume and internal energy, respectively. The values of these parameters are taken from Wang et al. [30]. On the basis of this model, the selected internal pressures correspond to TNT charge equivalents of 4.171 g (10 MPa), 10.429 g (25 MPa), 12.514 g (30 MPa), 14.600 g (35 MPa), 20.857 g (50 MPa), 31.286 g (75 MPa), 41.714 g (100 MPa), 62.567 g (150 MPa), and 83.324 g (200 MPa). In addition, the pipe geometric parameters in all test cases follow the baseline values listed in Table 1. Moreover, to simulate a deep-water environment, the ambient water pressure is set to P_w = 1 MPa. At the same time, for the convenience of analysis, we nondimensionalize the pressure parameters on the basis of P_w: $P_b^* = P_b/P_w$, $P_i^* = P_i/P_w$. Additionally, we nondimensionalize the size parameters on the basis of R_s, for example, $\delta^* = \delta/R_s$.

Figure 6 presents a comparison of the time evolution of bubble dynamics and the associated structural response under 4 representative initial pressures. Two distinct dynamic response regimes of the pipe can be observed: an elastic oscillation regime ($P_b^* \leq 30$) and an implosive collapse regime ($P_b^* \geq 35$). These regimes differ not only in the extent of deformation but also in the bubble shape, jet formation, and energy transfer patterns.

Specifically, at $P_b^* = 25$, the bubble exhibits quasispherical oscillations with only minor flattening at its lower boundary. The pipe undergoes elastic oscillations with decreasing amplitude. Neither significant denting nor irreversible deformation is observed. During the bubble collapse phase, the elastic rebound of the pipe provides an upward pushing effect on the lower bubble boundary. In this case, the bubble's impact on the pipe is limited, and the amplitude of pipe vibrations diminishes over time.

At $P_b^* = 50$, the interaction enters a transitional regime. In the early expansion phase, the bubble rapidly grows and emits a strong expansion wave. The impact of the expanding bubble induces a downward concavity on the upper surface of the pipe by t = 27 ms. As the bubble collapses, the pipe begins to rebound but fails to recover its original shape, marking the onset of large-scale plastic deformation. In the subsequent bubble re-expansion phase, the concavity on the pipe acts as a geometric trap, concentrating the bubble's loading on the midsection. This results in intensified deformation of the pipe, eventually resulting in a flattened collapse.

At $P_b^* = 75$, the bubble-pipe interaction exhibits a more intensified deformation process than that at $P_b^* = 50$. During the bubble expansion phase, a stronger expansion wave is produced, which leads to significant compression on the upper wall of the pipe. By t = 18.6 ms, a deeper downward concavity has formed. The bubble's lower boundary is pulled into a "bulb-like" shape. In the following process, despite not being subjected to the jet's direct impact, the pipe continues to deform inward owing to a buckling-folding instability, eventually resulting in a flattened and irreversible collapse. Notably, during the bubble's first expansion, the pipe's concavity acts as a geometric trap that focuses the expansion wave, leading to localized high-pressure accumulation. The focus of compressive energy at this concavity amplifies the downward load on the structure. At t = 37.2 ms, elastic rebound subsequently occurs in the

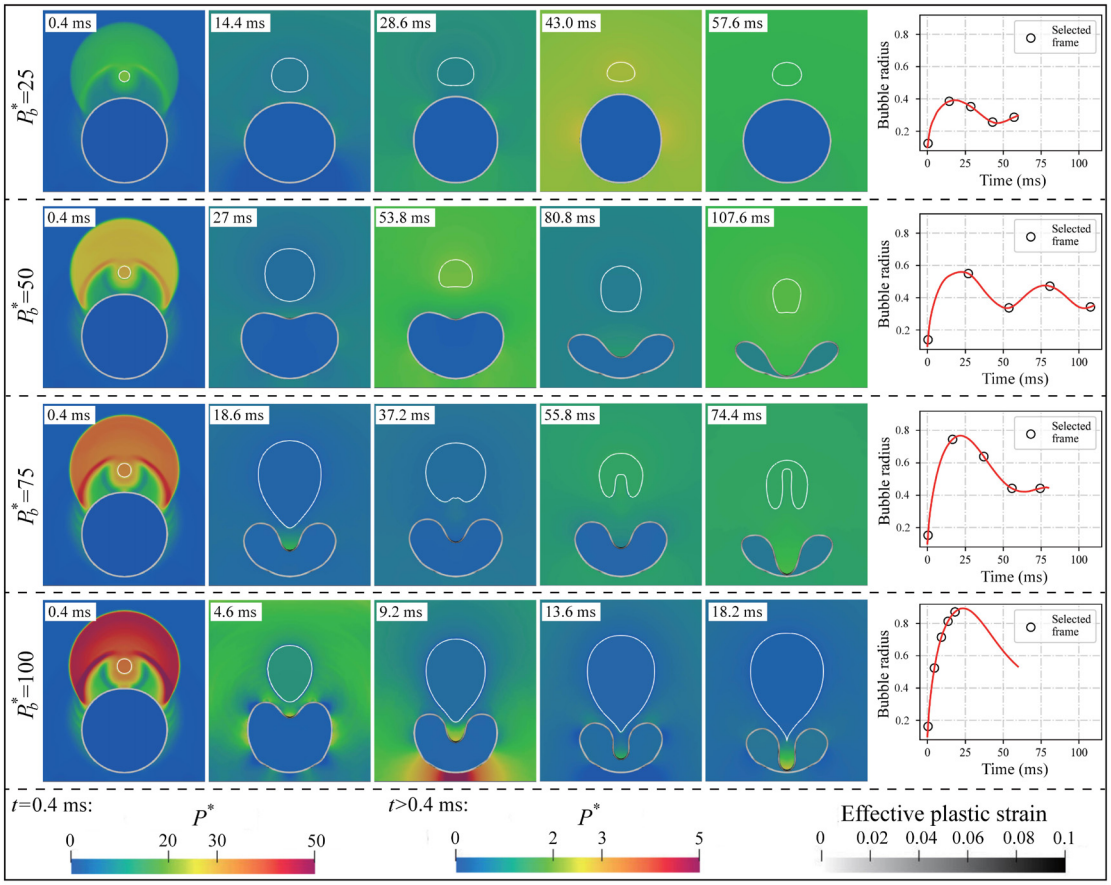

Fig. 6. Pressure contours of the bubble dynamics with pipes under 4 representative explosion pressures.

compressed region, imparting upward momentum to the lower bubble interface. This initiates the formation of a distinct upward-directed bubble jet, which becomes clearly visible at $t = 55.8$ ms. This jet illustrates a feedback mechanism in which structural deformation modifies the local pressure field of the bubble, reinforcing the two-way coupling between pipe collapse and bubble dynamics. A similar concavity-induced pressure accumulation can also be observed that at $P_b^* = 50$, the resulting pressure gradient during the second bubble cycle is relatively weak. At $t = 80.8$ ms, although the pipe collapse zone experiences elevated pressure, the reduced intensity and gradient are insufficient to trigger an upward jet.

At $P_b^* = 100$, the process accelerates significantly: the pipe enters plastic deformation almost immediately and collapses into a curly shape before the bubble completes its expansion. Unlike the lower-pressure cases, the process bypasses the typical rebound-collapse sequence entirely. Additionally, during collapse, the bubble's lower boundary is significantly elongated under a high-pressure gradient, forming a more pronounced "bulb-like" shape. Owing to the premature structural collapse of the pipe before the bubble completes its full expansion, no reverse jet is observed. However, a distinct high-pressure accumulation still forms at the concave region on the upper surface of the pipe. At $t = 9.2$ ms, the expanding bubble induces an early and intense pressure concentration in this region. Compared with lower-pressure scenarios, the focused pressure region emerges more rapidly and with greater intensity. From the above representative case, it is worth noting that in similar configurations, Ma et al. [9] observed three main deformation modes of pipes in the absence of rigid seabeds and structural supports: oscillation, axisymmetric collapse, and curling collapse. In our study, however, the presence of boundaries and supports inhibited the occurrence of axisymmetric collapse. These structural constraints limit large-scale displacement and deformation between supports, causing the impact to concentrate in localized regions and increasing the likelihood of asymmetric curling.

Interestingly, the rate and mode of pipe implosion vary considerably with the initial explosion pressure. To further quantify the morphological changes and dynamic mechanisms of pipe implosion, we compare several implosion-related parameters across the tested initial pressures. Figure 7(a) compares the final morphologies of the collapsed pipe. The changes of corresponding width and height with respect to the initial pressure are plotted in Fig. 7(c) and (d). As the initial pressure increases, the width decreases progressively whereas the height increases. These trends illustrate a transition from flat denting to narrow, deep folding as the bubble-induced loading intensifies. The change in the pipe's implosion time is illustrated in Fig. 7(b). It is expected that the implosion time decreases significantly as P_b^* increases.

The above results suggest a pressure-dependent transition in the implosion mechanism. When $P_b^* < 100$, the bubble's maximum volume and loading intensity are limited, preventing the pipe from implosing during the initial expansion phase. In this regime, implosion is driven primarily by the bubble's secondary collapse. Specifically, the second collapse generates a localized high-pressure region near the upper wall of the pipe, inducing downward deformation. The resulting morphology is typically a flattened, column-like shape. In contrast, when $P_b^* \geq 100$, the first expansion of the bubble is sufficient to trigger substantial implosive deformation. The implosion process becomes dominated by top collapse, while the pipe's sidewalls curl inward due to tensile effects. The implosion morphology gradually evolves into a shape characterized by minimal deformation at the ends and pronounced vertical compression at the center.

Furthermore, bubble migration and pipe deformation are critical for understanding the underlying fluid-structure interaction mechanisms [52,53]. Figure 8 presents the temporal evolution of three key

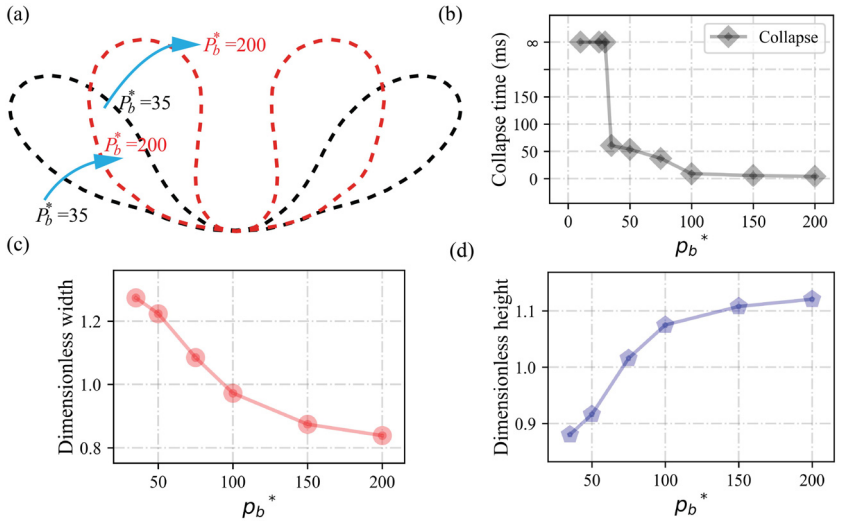

Fig. 7. (a) Pipe morphology, (b) pipe collapse time, (c) pipe width, and (d) pipe height when collapsing at different explosion pressures.

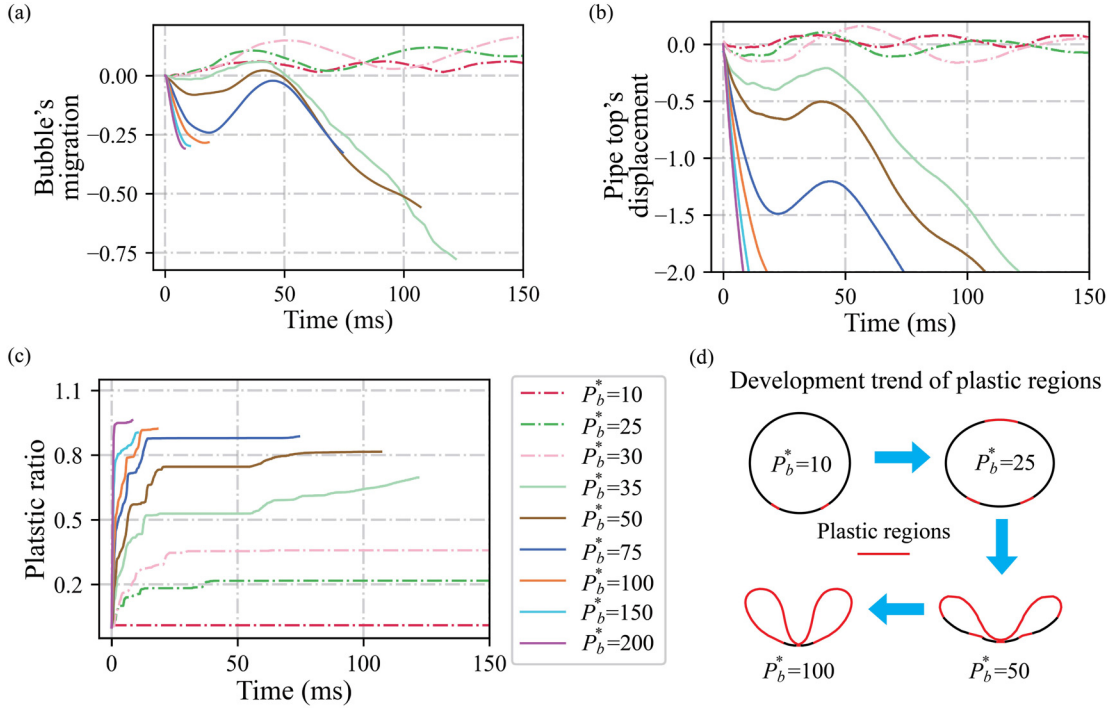

Fig. 8. (a) Bubble migration, (b) pipe top displacement, (c) pipe plastic ratio, and (d) pipe development trend of plastic regions at different explosion pressures.

indicators across a range of $P_b{}^*$ values: bubble centroid migration (Fig. 8(a)), pipe top displacement (Fig. 8(b)), and plastic zone development (Fig. 8(c)). The corresponding spatial distributions of the plastic regions are schematically summarized in Fig. 8(d).

As shown in Fig. 8(a), low-pressure cases ($P_b{}^*$ = 10, 25, and 30) exhibit periodic centroid oscillations with short durations and limited amplitudes, reflecting restrained bubble expansion due to lower energy release. Among them, $P_b{}^*$ = 10 features the shortest period and smallest amplitude, resulting from its minimal internal pressure, which restricts the bubble volume. The bubble remains nearly spherical, generating symmetric pressure waves and resulting in limited structural impact. These periodic motions induce synchronized oscillations in the pipe top displacement (Fig. 8(b)). As depicted in Fig. 8(c), $P_b{}^*$ = 10 produces negligible deformation, with the plastic strain remains near zero. In contrast, $P_b{}^*$ = 30 triggers localized plasticity due to larger displacements near the bubble-facing apex, where alternating bending stresses begin to exceed yield thresholds.

At intermediate pressures ($P_b{}^*$ = 35, 50, and 75), the system becomes significantly more complex and nonlinear. The centroid trajectory becomes nonmonotonic, descends initially, briefly rebounds upward, and then accelerates downward again. This reflects a two-stage interaction: during initial expansion, the bubble induces localized pipe concavity without full collapse, which compresses the lower bubble surface and causes the reverse jet. Additionally, this rebound is mirrored in the displacement of the pipe top (Fig. 8(b)), which shows initial downward motion, brief elastic recovery, and subsequent intensified deflection. As the energy input increases, elastic recovery becomes less effective and plastic deformation initiates earlier, as confirmed by the rapid rise in plastic strain (Fig. 8(c)). Particularly for $P_b{}^*$ = 75, the plastic ratio escalates quickly and saturates at a relatively high level, indicating reduced struc-

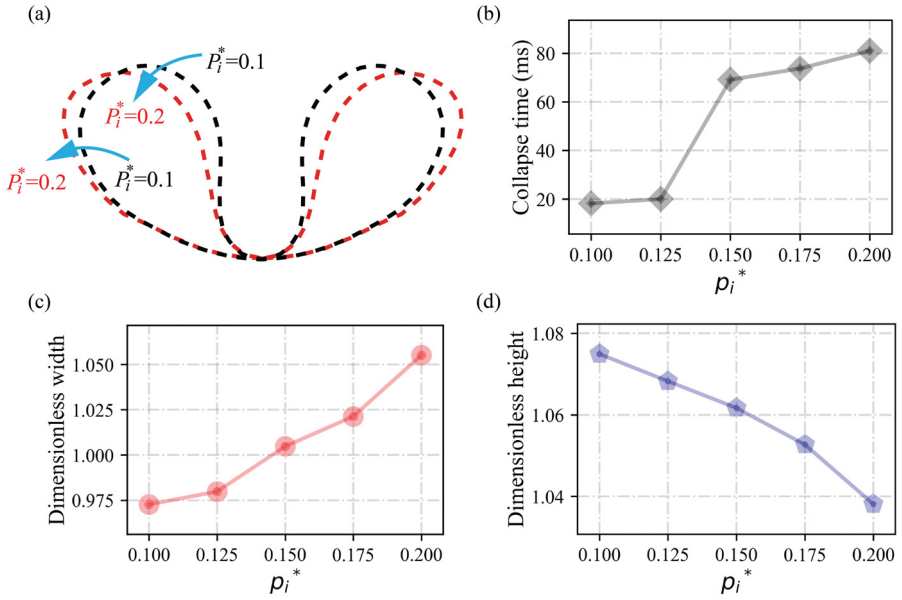

Fig. 9. (a) Pipe morphology, (b) pipe collapse time, (c) pipe width, and (d) pipe height when the pipe collapses at different inner pressures.

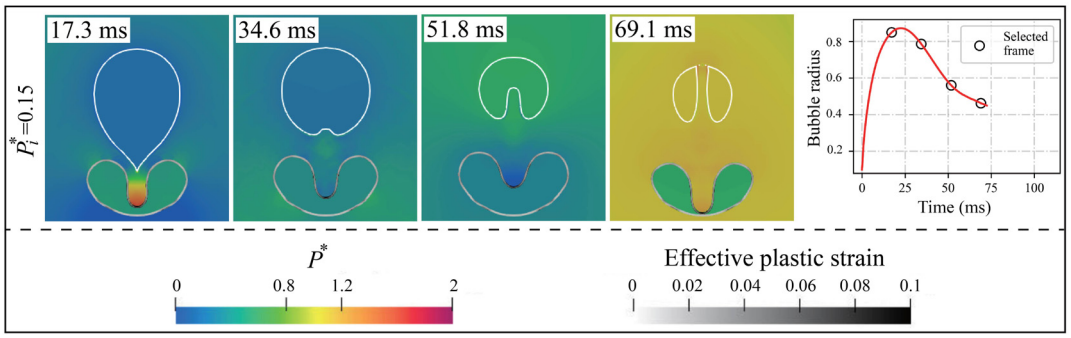

Fig. 10. Pressure contours of the bubble dynamics with the pipe at P_i^*=0.15.

tural recoverability under relatively strong fluid-structure coupling. In the high-pressure regime (P_b^* = 100 and above), asymmetric collapse dominates. The bubble centroid follows a sharp, monotonic descent toward the structure with no rebound, signifying direct impact. With increasing P_b^*, the centroid's downward velocity, pipe deflection rate, and structural failure onset all intensify. The pipe top rapidly reaches a normalized displacement of −2, indicating complete implosion.

Figure 8 (d) further reveals the spatial evolution of the plastic zones with increasing pressure. At P_b^* = 10, plastic deformation is negligible and limited to regions near the supports. When P_b^* = 25, the plasticity extends toward the apex, reflecting accumulated stress from repeated oscillations. At P_b^* = 50, the plastic deformation becomes more pronounced across the top wall, with the central region fully yielding. However, the collapse pattern remains relatively flat, resulting in partial preservation of elasticity near the flanks. When P_b^* = 100, the entire upper span between the supports is almost completely plastified, leaving only narrow bands between the supports that remain elastic.

4. Parametric analysis and discussion

To further investigate the structural behavior of the pipe under varying operating and design conditions, we conduct a series of parametric studies based on the baseline case with P_b^* = 100. Specifically, the effects of the internal pipe pressure, wall thickness, and support angle are analyzed. Unless otherwise specified, all the geometric and explosion parameters follow the baseline configuration listed in Table 1, and only the parameter under investigation is varied in each case.

4.1. Effects of pipe internal pressure

We first investigate the effects of the initial internal pressure of the pipe. Five different values are tested: P_i^* = 0.1, 0.125, 0.15, 0.175, and 0.2. The results are compared in Fig. 9. The results show that the pipe's collapse time increases significantly with increasing internal pressure (Fig. 9(b)). This is expected because a higher internal pressure can increase the resistance of a pipe to deformation. One interesting observation occurs at P_i^* = 0.15: at this pressure level, the first bubble expansion fails to trigger pipe implosion. Instead, the collapse of the pipe is driven primarily by the bubble's second pulsation, resulting in a significant increase in the collapse time.

Figure 9(a) compares the final pipe morphologies after collapse. As shown in Fig. 9(c) and (d), increasing the internal pressure leads to an increase in width, whereas the height tends to decrease progressively. This morphological shift indicates a redistribution of the strain and deformation: at lower internal pressures, the impact of the bubble is concentrated at the pipe's upper-central region, forming a narrow and deep concavity. However, as the internal pressure increases, the internal support mitigates localized collapse and results in a broader, flatter shape (Fig. 10).

Similarly, we further expand and analyze the mechanism between bubble migration and pipe deformation. As shown in Fig. 11(a) and

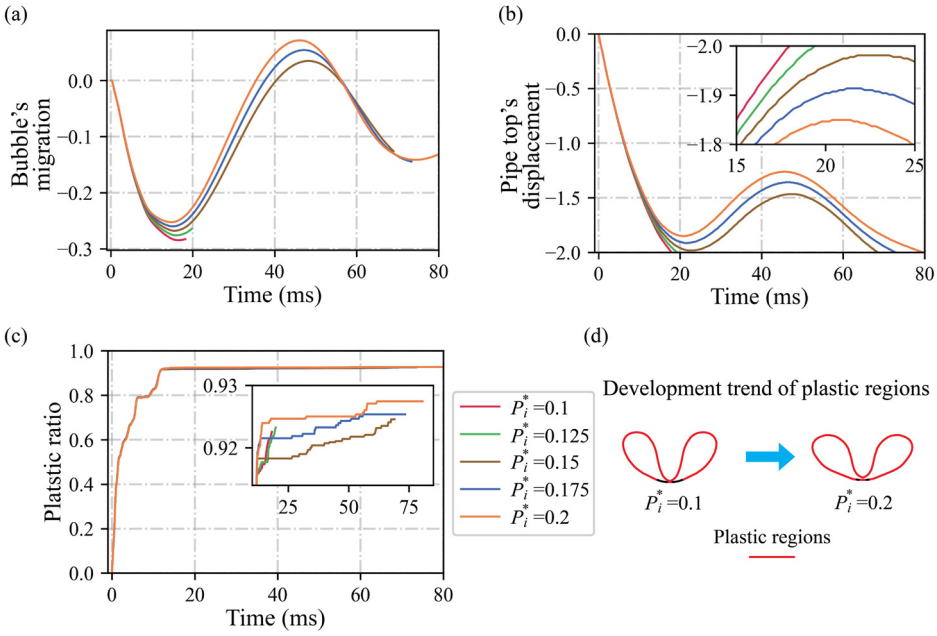

Fig. 11. (a) Bubble migration, (b) pipe top displacement, (c) pipe plastic ratio, and (d) pipe development trend of plastic regions at different pipe inner pressures.

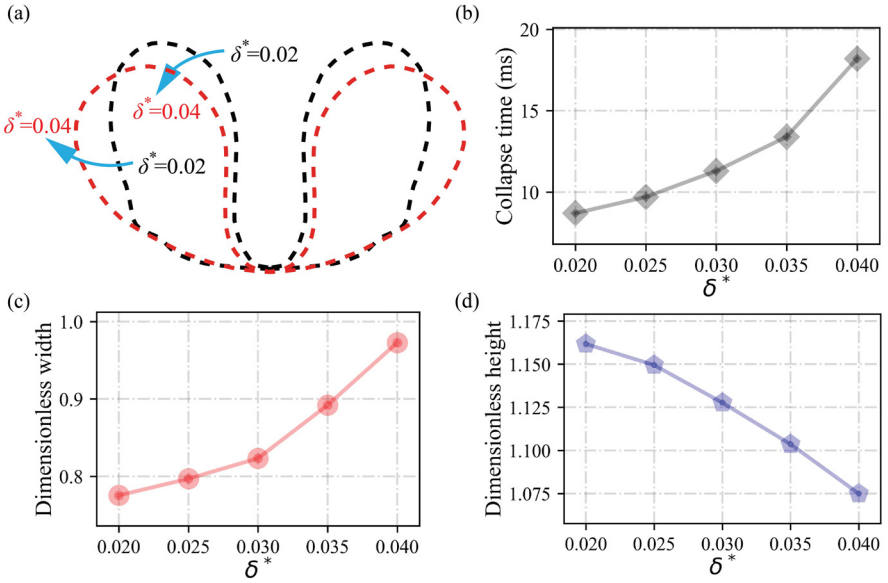

Fig. 12. (a) Pipe morphology, (b) pipe collapse time, (c) horizontal displacement, and (d) pipe vertical displacement when collapsing at different values of pipe thickness.

(b), when $P_i^* \leq 0.15$, the lack of internal resistance results in pipe failure during the initial expansion of the bubble. The bubble centroid exhibits rapid downward migration with a large amplitude, and the pipe top undergoes a sharp, nonrecoverable collapse. In contrast, a higher P_i^* allows the pipe to deform elastically and rebound, compressing the trapped fluid and inducing an upward shift of the bubble. This fluid-structure feedback defers collapse to the second pulsation, explaining the delayed structural failure and flatter morphologies observed in Fig. 9. The associated plastic evolution (Fig. 11(c) and (d)) further supports this transition. Although all the cases exhibit initial plastic growth from shock and expansion, their long-term responses diverge. At low P_i^*, early curled implosion causes steep plastic accumulation prior to full collapse. At higher P_i^*, collapse during the second pulsation results in a flattened geometry and compressive squeezing between the supports, broadening the plastic regions through constrained deformation and stress redistribution.

4.2. Effects of pipe thickness

We then examine the effect of the pipe thickness on the bubble-pipe interaction. Five thickness values are tested: $\delta^* = 0.02$, 0.025, 0.03, 0.035, and 0.04. Across all the cases, the pipe implodes during the bubble's first expansion cycle, but the timing of collapse clearly depends on the wall thickness. As shown in Fig. 12(b), the collapse time decreases nonlinearly with decreasing δ^*. This reflects the enhanced structural stiffness and inertia of thicker walls, which delay the onset of instability. Notably, reducing the thickness from the baseline $\delta^* = 0.04$ to $\delta^* = 0.02$ nearly doubles the collapse speed. These results indicate that pipe thickness is a key design variable with strong effects on implosion dynamics.

The changes in implosion morphology (Fig. 12(a)) further reveal the effects of pipe thickness. For thinner pipes, the deformation is concentrated at the top center, forming a deep local concavity due to weak

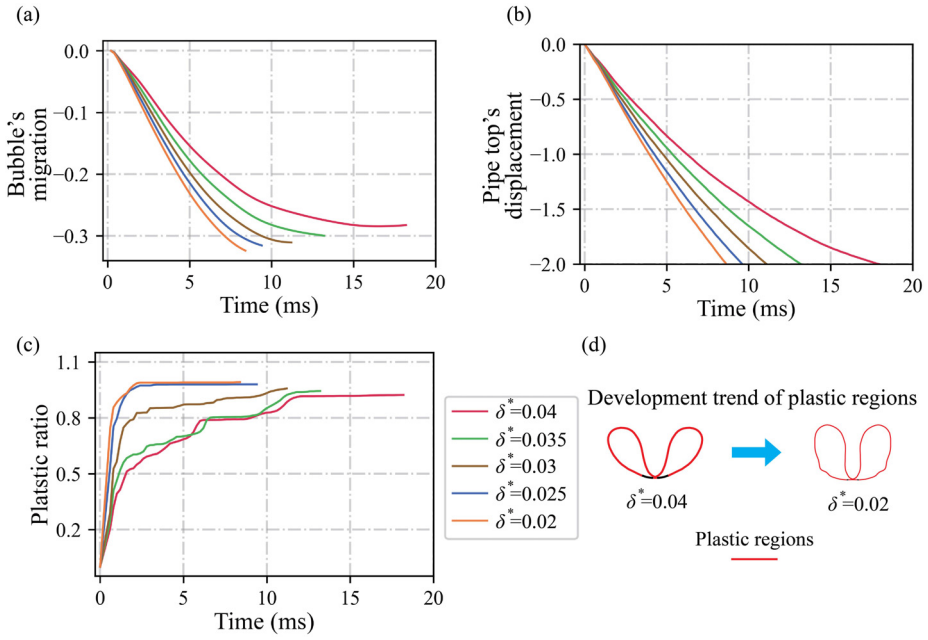

Fig. 13. (a) Bubble migration, (b) pipe top displacement, (c) pipe plastic ratio, and (d) pipe development trend of plastic regions at different pipe thickness.

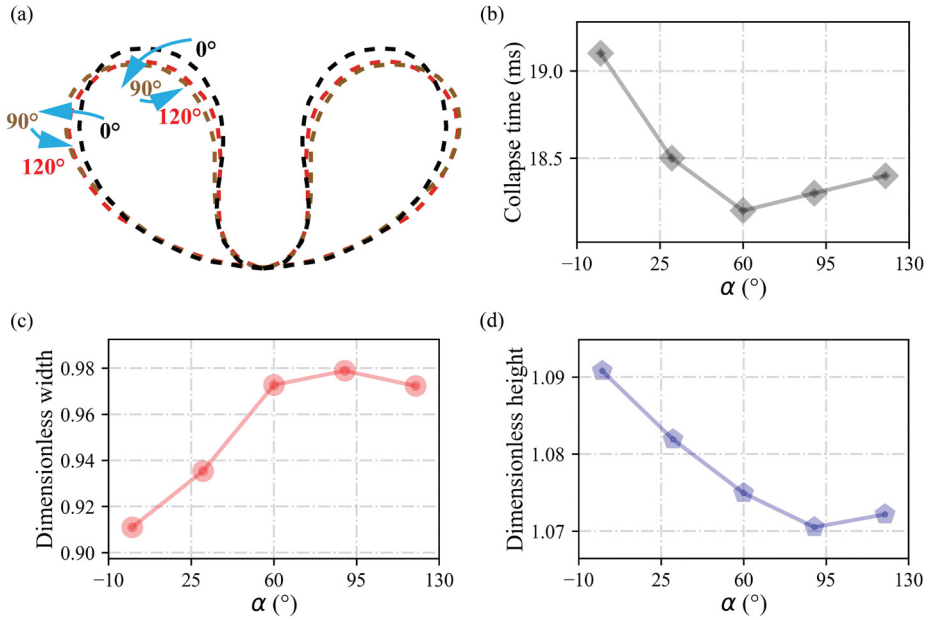

Fig. 14. (a) Pipe morphology, (b) pipe collapse time, (c) pipe width, and (d) pipe height when collapsing at different support angles.

structural resistance. In contrast, thicker the pipes exhibit a more flattened profile with reduced localized deformation, indicating a better load distribution. This trend is further supported by Fig. 12(c) and (d), where the postcollapse width increases and the height decreases with thickness.

As shown in Fig. 13(a) and (b), thinner pipes exhibit more rapid bubble migration and greater top-wall displacement within the same timeframe. A reduced structural stiffness permits easier deformation under bubble-induced pressure, leading to earlier and more pronounced structural responses. Conversely, increased inertia and rigidity in thicker pipes suppress deformation and limit bubble movement, which is consistent with the delayed collapse and flattened profiles in Fig. 12(b). The corresponding plastic theoretical ratio evolution is shown in Fig. 13(c). For thinner walls, plastic strain accumulates quickly and reaches higher saturation, indicating early material yielding and curl-induced failure. Thicker walls exhibit slower plastic growth and lower final plasticity, reflecting improved structural resistance under impulsive loading. In thinner pipes, low stiffness may further induce spanwise instability, resulting in local compression, buckling, and additional plastic deformation between supports.

4.3. *Effects of the support angle*

Next, we investigate the effects of the support angle. Five different values are tested: $\alpha = 0°$, $30°$, $60°$, $90°$, and $120°$. Variations in the support angle significantly influence the force distribution and dynamic response of the pipe by altering its longitudinal and lateral stiffness.

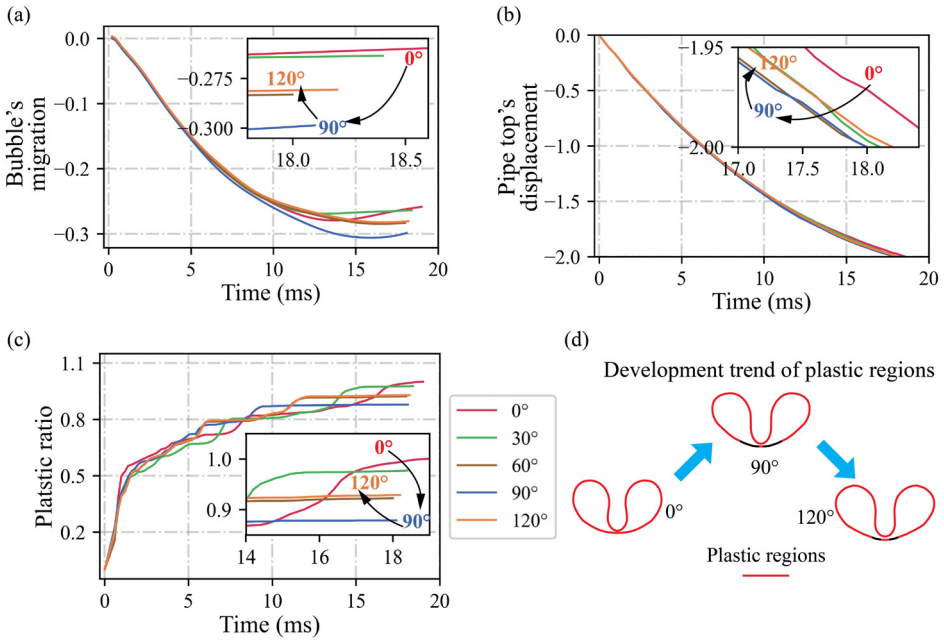

Fig. 15. (a) Bubble migration, (b) pipe top displacement, (c) pipe plastic ratio, and (d) pipe development trend of plastic regions at different support angles.

Figure 14 (b) shows that the collapse time exhibits a nonmonotonic "U-shaped" trend with increasing support angle. At smaller support angles (0°, 30°), the supports are positioned close together under the pipe, providing strong longitudinal stiffness to the pipe. This delays the onset of collapse, as higher pressure is required to initiate deformation. When $\alpha = 60°$, the support becomes less effective in both the longitudinal and lateral directions, leading to a significant pressure concentration effect in the top region. This facilitates rapid local collapse, and the collapse time reaches a minimum. Beyond $\alpha = 60°$, the supports move farther outward, improving the lateral stiffness. This reduces the deformation rate and causes the collapse time to increase again.

Compared with the pipe thickness, the support angle has a limited effect on the final pipe morphology. As shown in Fig. 14(a), (c), and (d), the width increases slightly with the support angle and then remains nearly unchanged after 60°, whereas the height decreases only slightly. Hence, the overall dynamic response of the pipe remains relatively insensitive to the support angle. As shown in Fig. 15(a)–(d), the variations in bubble migration, pipe top displacement, and the plastic ratio are minimal across different support angles.

5. Conclusions

This study develops a fluid-structure coupling simulation framework by integrating a multiphase compressible fluid dynamics solver with a nonlinear structural dynamics solver. By examining the flow field, bubble dynamics, and transient stress-strain responses of the pipe, the interactions between the bubble, the surrounding water, and the pipe are thoroughly analyzed. In contrast to most previous studies based on idealized models [9], this work accounts for three critical factors relevant to practical applications: seabed constraints, the two-way interaction between bubble dynamics and the pipe response, and structural support configurations.

First, we investigate the pipe response under different explosion pressures (10 MPa, 4.171 g of TNT → 200 MPa, 83.324 g of TNT) and identify two response types: periodic oscillation (≤30 MPa, 12.514 g of TNT) and downward collapse (≥35 MPa, 14.6 g of TNT). At lower initial pressures, the bubble expansion pressure is weak, resulting in only minor elastic responses of the pipe without significant plastic deformation. At moderate initial pressures, significant concavities are observed at the top of the pipe, which lead to plastic deformation under the influence of bubble pulses. At higher initial pressures, the strong pressure waves and jets emitted by bubble pulsation act together, causing rapid pipe implosion characterized by significant collapse from the top surface. In addition, as the initial pressure increases, the bubble's lower edge elongates during the expansion phase, forming a characteristic "bulb-like" shape, whereas the jet intensity, and the pressure wave amplitude increases significantly. The pipe deformation transitions from overall flat compression to vertical compression at the center, with the implosion time decreasing progressively. Simultaneously, analysis of bubble migration and structural plastic deformation reveals that the pipe's concavity acts as a geometric trap, concentrating compressive energy and leading to localized pressure amplification in the fluid. The subsequent elastic rebound of the structure destabilizes the lower bubble interface, triggering the formation of the reverse jet.

We subsequently conduct a systematic analysis of factors such as the internal pipe pressure ($1 \times 10^5 \rightarrow 2 \times 10^5$ Pa), wall thickness (10→20 mm) and support angle (0° → 120°) to reveal the dynamic response characteristics of the pipe under different conditions. Increasing the internal pressure markedly delays collapse and redistributes deformation, transitioning from top-localized collapse to a flatter mode with increased width and reduced height. For pipe thickness, thinner pipes feature localized top denting, whereas thicker pipes exhibit greater resistance and more uniform deformation, along with prolonged collapse times. The support angle introduces a nonmonotonic effect: the collapse time initially decreases and then reaches a minimum at 60°. These findings provide valuable insights into the structural design of submarine pipelines for enhancing the resistance to explosive loading.

Declaration of competing interest

The authors declare that they have no known competing financial interests or personal relationships that could have appeared to influence the work reported in this paper.

CRediT authorship contribution statement

Lei Gao: Visualization, Validation, Data curation. **Junjie Zhao:** Visualization, Methodology, Validation, Investigation, Writing – original

draft, Software, Formal analysis. **Maoyu Qi:** Validation, Software, Writing – original draft. **Wentao Ma:** Software, Resources. **Shunxiang Cao:** Supervision, Software, Writing – review & editing, Funding acquisition.

Acknowledgments

This work was supported by the National Key R&D Program of China (Grant No. 2024YFC3013200) and the Shenzhen Peacock Plan (Grant No. QD2023006C).

References

[1] X. Li, G. Chen, H. Zhu, Quantitative risk analysis on leakage failure of submarine oil and gas pipelines using Bayesian network, Process Saf. Environ. Prot. 103 (2016) 163–173.
[2] J. Elger, C. Berndt, L. Rüpke, S. Krastel, F. Gross, W.H. Geissler, Submarine slope failures due to pipe structure formation, Nat. Commun. 9 (1) (2018) 715.
[3] B. Zhang, R. Gong, T. Wang, Z. Wang, Causes and treatment measures of submarine pipeline free-spanning, J. Mar. Sci. Eng. 8 (5) (2020) 329.
[4] T.-k. Nian, X.-l. Song, W. Zhao, H.-b. Jiao, X.-s. Guo, Submarine slope failure due to overpressure fluid associated with gas hydrate dissociation, Environ. Geotech. 9 (2) (2020) 108–123.
[5] Y. Chen, S. Wang, Y. Hao, K. Yao, H. Li, F. Jia, D. Yue, Q. Shi, Y. Cheng, X. Huang, Temperature monitoring for 500 kv oil-filled submarine cable based on BOTDA distributed optical fiber sensing technology: Method and application, IEEE Trans. Instrum.Meas. 71 (2021) 1–10.
[6] T. Wu, N. Jiang, C. Zhou, X. Luo, J. Sun, Evaluate of anti-explosion for high-pressure gas steel pipeline subjected to ground explosion, J. Constr. Steel Res. 177 (2021) 106429.
[7] N.K. Gupta, et al., Response of thin walled metallic structures to underwater explosion: a review, Int. J. Impact Eng. 156 (2021) 103950.
[8] Z. Liu, Y.L. Young, Transient response of submerged plates subject to underwater shock loading: an analytical perspective, J. Appl. Mech. 75 (4) (2008) 044504.
[9] W. Ma, X. Zhao, C. Gilbert, K. Wang, Computational analysis of bubble–structure interactions in near-field underwater explosion, Int. J. Solids. Struct. 242 (2022) 111527.
[10] A.K. Mathew, Modeling Underwater Explosion (UNDEX) Shock Effects for Vulnerability Assessment in Early Stage Ship Design, Virginia Tech, 2018 Ph.D. thesis.
[11] J.L. O'Daniel, T. Krauthammer, K.L. Koudela, L.H. Strait, An UNDEX response validation methodology, Int. J. Impact Eng. 27 (9) (2002) 919–937.
[12] H. Wang, X. Zhu, Y.S. Cheng, J. Liu, Experimental and numerical investigation of ship structure subjected to close-in underwater shock wave and following gas bubble pulse, Mar. Struct. 39 (2014) 90–117.
[13] Z.F. Zhang, C. Wang, L.K. Wang, A.M. Zhang, V.V. Silberschmidt, Underwater explosion of cylindrical charge near plates: analysis of pressure characteristics and cavitation effects, Int. J. Impact Eng. 121 (2018) 91–105.
[14] K. Mäkinen, Cavitation models for structures excited by a plane shock wave, J. Fluids Struct. 12 (1) (1998) 85–101.
[15] J.M. Brett, G. Yiannakopoulos, P.J. Van der Schaaf, Time-resolved measurement of the deformation of submerged cylinders subjected to loading from a nearby explosion, Int. J. Impact Eng. 24 (9) (2000) 875–890.
[16] J.M. Brett, G. Yiannakopolous, A study of explosive effects in close proximity to a submerged cylinder, Int. J. Impact Eng. 35 (4) (2008) 206–225.
[17] G. Li, D. Shi, L. Wang, K. Zhao, Measurement technology of underwater explosion load: a review, Ocean Eng. 254 (2022) 111383.
[18] S. Gupta, H. Matos, J.M. LeBlanc, A. Shukla, Shock initiated instabilities in underwater cylindrical structures, J. Mech. Phys. Solids 95 (2016) 188–212.
[19] J. LeBlanc, C. Shillings, E. Gauch, F. Livolsi, A. Shukla, Near field underwater explosion response of polyurea coated composite plates, Exp. Mech. 56 (2016) 569–581.
[20] C. Javier, M. Galuska, M. Papa, J. LeBlanc, H. Matos, A. Shukla, Underwater explosive bubble interaction with an adjacent submerged structure, J. Fluids Struct. 100 (2021) 103189.
[21] A.P. Mouritz, Advances in understanding the response of fibre-based polymer composites to shock waves and explosive blasts, Compos. Part A Appl. Sci. Manuf. 125 (2019) 105502.
[22] P. Wanchoo, H. Matos, C.-E. Rousseau, A. Shukla, Investigations on air and underwater blast mitigation in polymeric composite structures–a review, Compos. Struct. 263 (2021) 113530.
[23] S.E. Turner, J.M. Ambrico, Underwater implosion of cylindrical metal tubes, J. Appl. Mech. 80 (1) (2013) 011013.
[24] S. Kishore, P. Naik Parrikar, N. DeNardo, A. Shukla, Underwater dynamic collapse of sandwich composite structures, Exp. Mech. 59 (2019) 583–598.
[25] C.M. Ikeda, J. Wilkerling, J.H. Duncan, The implosion of cylindrical shell structures in a high-pressure water environment, Proc. R. Soc. A Math. Phys. Eng. Sci. 469 (2160) (2013) 20130443.
[26] T. Muttaqie, S.H. Park, J.M. Sohn, S.-R. Cho, I.S. Nho, S. Han, P.-S. Lee, Y.S. Cho, Experimental investigations on the implosion characteristics of thin cylindrical aluminium-alloy tubes, Int. J. Solids. Struct. 200 (2020) 64–82.
[27] W. Sun, T. Zhu, P. Chen, G. Lin, Dynamic implosion of submerged cylindrical shell under the combined hydrostatic and shock loading, Thin-Walled Struct. 170 (2022) 108574.
[28] W.-s. Mao, M.-s. Zhong, X.-b. Xie, H.-y. Ma, G.-l. Yang, L. Fan, Research on the dynamic response of pressurized cylindrical shell structures subjected to a near-field underwater explosion, AIP Adv. 13 (2) (2023) 025046.
[29] W.-s. Mao, M.-s. Zhong, X.-b. Xie, H.-y. Ma, G.-l. Yang, L. Fan, Dynamic response of a hollow cylindrical shell subjected to a near-field underwater explosion, J. Appl. Phys. 135 (22) (2024).
[30] F. Wang, S. Li, Numerical investigation of concrete-filled double skin steel tubular (CFDST) structure subjected to underwater explosion loading, Mar. Struct. 90 (2023) 103427.
[31] A.M. Zhang, W.B. Wu, Y.L. Liu, Q.X. Wang, Nonlinear interaction between underwater explosion bubble and structure based on fully coupled model, Phys. Fluids 29 (8) (2017) 082111.
[32] K. Zhao, N. Jiang, C. Zhou, H. Li, Z. Cai, B. Zhu, Dynamic behavior and failure of buried gas pipeline considering the pipe connection form subjected to blasting seismic waves, Thin-Walled Struct. 170 (2022) 108495.
[33] K.Y. Lam, Z. Zong, Q.X. Wang, Dynamic response of a laminated pipeline on the seabed subjected to underwater shock, Compos. Part B Eng. 34 (1) (2003) 59–66.
[34] K.G. Wang, P. Lea, C. Farhat, A computational framework for the simulation of high-speed multi-material fluid–structure interaction problems with dynamic fracture, Int. J. Numer. MethodsEng. 104 (7) (2015) 585–623.
[35] S. Cao, A. Main, K.G. Wang, Robin-Neumann transmission conditions for fluid-structure coupling: embedded boundary implementation and parameter analysis, Int. J. Numer. MethodsEng. 115 (5) (2018) 578–603.
[36] C. Farhat, K.G. Wang, A. Main, S. Kyriakides, L.-H. Lee, K. Ravi-Chandar, T. Belytschko, Dynamic implosion of underwater cylindrical shells: Experiments and computations, Int. J. Solids. Struct. 50 (19) (2013) 2943–2961.
[37] B. Van Leer, Towards the ultimate conservative difference scheme. v. a second-order sequel to Godunov's method, J. Comput. Phys. 32 (1) (1979) 101–136.
[38] P.L. Roe, Approximate Riemann solvers, parameter vectors, and difference schemes, J. Comput. Phys. 43 (2) (1981) 357–372.
[39] C. Farhat, A. Rallu, K. Wang, T. Belytschko, Robust and provably second-order explicit–explicit and implicit–explicit staggered time-integrators for highly non-linear compressible fluid–structure interaction problems, Int. J. Numer. MethodsEng. 84 (1) (2010) 73–107.
[40] K. Wang, A. Rallu, J.-F. Gerbeau, C. Farhat, Algorithms for interface treatment and load computation in embedded boundary methods for fluid and fluid–structure interaction problems, Int. J. Numer. MethodsFluids 67 (9) (2011) 1175–1206.
[41] S. Cao, Y. Zhang, D. Liao, P. Zhong, K.G. Wang, Shock-induced damage and dynamic fracture in cylindrical bodies submerged in liquid, Int. J. Solids. Struct. 169 (2019) 55–71.
[42] S. Cao, D. Zhengyu Huang, Bayesian calibration for large-scale fluid structure interaction problems under embedded/immersed boundary framework, Int. J. Numer. MethodsEng. 123 (8) (2022) 1791–1812.
[43] M.R. Bailey, A.D. Maxwell, S. Cao, S. Ramesh, Z. Liu, J.C. Williams, J. Thiel, B. Dunmire, T. Colonius, E. Kuznetsova, et al., Improving burst wave lithotripsy effectiveness for small stones and fragments by increasing frequency: theoretical modeling and ex vivo study, J.Endourol. 36 (7) (2022) 996–1003.
[44] G. Xiang, X. Ma, C. Liang, H. Yu, D. Liao, G. Sankin, S. Cao, K. Wang, P. Zhong, Variations of stress field and stone fracture produced at different lateral locations in a shockwave lithotripter field, J. Acoust. Soc. Am. 150 (2) (2021) 1013–1029.
[45] W. Ma, X. Zhao, S. Islam, A. Narkhede, K. Wang, Efficient solution of Bimaterial Riemann problems for compressible multi-material flow simulations, J. Comput. Phys. 493 (2023) 112474.
[46] K.G. Wang, P. Lea, A. Main, O. McGarity, C. Farhat, Predictive simulation of underwater implosion: coupling multi-material compressible fluids with cracking structures, in: International Conference on Offshore Mechanics and Arctic Engineering, volume 45509, American Society of Mechanical Engineers, 2014. V08AT06A028
[47] X. Zhao, W. Ma, J. Chen, G. Xiang, P. Zhong, K. Wang, Vapour bubbles produced by long-pulsed laser: a race between advection and phase transition, J. Fluid Mech. 999 (2024) A103.
[48] W. Ma, X. Zhao, C. Gilbert, K. Wang, Numerical simulation data of bubble-structure interactions in near-field underwater explosion, Data Brief 43 (2022) 108337.
[49] K. Wang, J. Grétarsson, A. Main, C. Farhat, Computational algorithms for tracking dynamic fluid–structure interfaces in embedded boundary methods, Int. J. Numer. MethodsFluids 70 (4) (2012) 515–535.
[50] C.M. Ikeda, Fluid Structure Interactions: Implosions of Shell Structures and Wave Impact on a Flat Plate, University of Maryland, College Park, 2012.
[51] D. Mohotti, K. Wijesooriya, S. Weckert, A simplified approach to modelling blasts in computational fluid dynamics (CFD), Def. Technol. 23 (2023) 19–34.
[52] A.-M. Zhang, S.-M. Li, P. Cui, S. Li, Y.-L. Liu, Interactions between a central bubble and a surrounding bubble cluster, Theor. Appl. Mech. Lett. 13 (3) (2023) 100438.
[53] J. Zhao, P. Bai, J. Wang, Y. Wang, S. Cao, Dynamics of bubble collapse near rigid boundaries with different curvatures, Phys. Fluids 37 (3) (2025).